CHALMERS
UNIVERSITY OF TECHNOLOGY

Scale resolving simulations of the non-cavitating and cavitating flows in an axial water jet pump

33rd Symposium on Naval Hydrodynamics
Osaka, Japan, 19 October-23 October 2020

Scale Resolving Simulations of the Non-cavitating and Cavitating Flows in an Axial Water Jet Pump

M.H. Arabnejad[1], A. Eslamdoost[1], U. Svennberg[2], and R.E. Bensow[1]
([1]Department of Mechanics and Maritime Sciences, Chalmers University of Technology, Gothenburg, Sweden, [2]Kongsberg Maritime Sweden AB, Kristinehamn, Sweden)

ABSTRACT

In this paper, the non-cavitating and cavitating flows in the AxWJ-2 axial water jet pump of Johns Hopkins University are simulated using a Large Eddy Simulation (LES) approach. The non-cavitating simulations are performed on grids with different mesh resolutions and the effect of mesh resolution on predicting the performance and capturing the structure of Tip Leakage Vortex (TLV) is investigated. Based on this investigation, it can be concluded that the main feature of the non-cavitating TLV can be well captured compared with the experiment provided that a refinement region with at least 40 cells in tip gap is used. The cavitating simulation using the same grid refinement also shows that the cavitating structures described in the experiment are predicted by the simulation. Furthermore, the structure of non-cavitating and cavitating TLVs are compared and the effect of cavitation on the structure of TLV are analysed using the simulation results.

INTRODUCTION

High-speed vessels and vessels designed to operate in shallow water are mostly equipped with water jet propulsion systems. To maximize the performance in this type of propulsion system, hydrodynamic cavitation in different components of the system is unavoidable. One region with high probability of cavitation is the Tip Leakage Vortex (TLV) formed at the tip of impeller blades in the water jet pump. This type of vortex forms as the result of an interaction between the leakage flow, a flow from the pressure side of a rotating impeller blade to its suction side, and the upstream flow. This interaction is shown in Figure 1. Due to high rotation in TLVs, pressure may drop locally below vapor pressure leading to formation of cavitating structures in TLV. Previous experimental studies (Tan et al., 2015; Laborde et al., 1997; Avellan, 2004) have shown that the formation of TLVs and their resultant cavitating structures in a pump are responsible for the onset of cavitation breakdown and a high-level of noise and vibration in pumps, therefore both numerical and experimental studies have been devoted to investigating non-cavitating and cavitating TLVs.

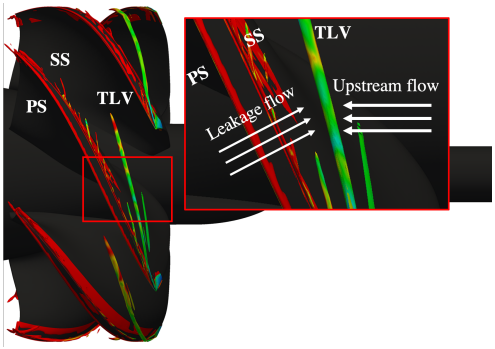

Figure 1: Formation of Tip leakage vortex.

A set of experimental studies examined the structure of TLVs and their associated cavitating structures. Wu et al. (2011, 2012) and Miorini et al. (2012) investigated the flow structures and turbulence of a TLV formed in an axial water jet pump using Particle Image Velocimetry (PIV) measurements. Their detailed analysis revealed that vortical structures, shed from the blade tip, wrap around each other and form the core of the TLV. As the main vortex migrates in the blade passage, it becomes stronger due to more entrainment of these vortical structures. Tan et al. (2012) showed that cavitation can form around the core of the TLV where the pressure is low. They also showed that by lowering the cavitation number, sheet cavitation forms which covers the suction side of the rotor blade. Tan et al. (2015) investigated the relation between cavitation dynamics and cavitation breakdown in an axial water jet pump using high-speed visualization and performance and pressure

measurements. Their investigation showed that cavitation breakdown occurs when cavitating vortices perpendicular to the suction side of one blade extend to the pressure side of the neighboring blade. These cavitating vortices are created due to the interaction between the cloudy structures formed at the closure line of the sheet cavity on the blade suction side and the cavitating TLV. Laborde et al. (1997) experimentally investigated the effect of the tip clearance geometry, tip gap height, and rotor blade geometry on the cavitating TLV. They observed less tip cavitation in TLV when the tip clearance edge of the rotor blade in the pressure side is rounded. They also showed that the cavitation pattern in the tip gap can be altered if the rotor blade is skewed backward or forward.

In addition to experimental studies, a few numerical studies have examined non-cavitating and cavitating TLVs in water jet pumps. Zhang et al. (2015c) numerically studied the effect of flow rate on the tip leakage flow and TLV in an axial pump. Their results showed that the change in the flow rate leads to a variation of blade loading and also change in the pressure difference between the pressure side and suction side at the tip which in turn results in the change in the starting point and the trajectory of TLV. Zhang et al. (2015b) investigated the cavitating structures formed in the tip gap of an axial water jet pump using numerical simulations. They demonstrated that four types of cavitating structures are formed in the gap region. These structures are the cavitating vortex formed in the tip clearance corner near the pressure side, cavitation formed in the high shear region between the rotor tip and stationary rotor casing, cavitation in the high shear region due to the wall jet flow, and cavitating TLV. Zhang et al. (2015a) studied the cavitating flow inside an axial water jet pump using Reynolds Averaged Navier-Stokes (RANS) approach. They investigated the generation mechanisms of Suction Side Perpendicular Cavitating Vortex (SSPCV). These structures were identified by Tan et al. (2015) as a possible mechanism which triggers cavitation breakdown in water jet pumps. Similar to Tan et al. (2015), they concluded that SSPCV structures are formed due to an interaction between the sheet cavity on the suction side of the blade and the cavitating TLV. They also showed that tip leakage flow close to the trailing edge of the rotor blade controls the orientation of SSPCV. Feng et al. (2016) studied the effect of tip clearance on the pressure fluctuation and the flow field in the rotor of an axial pump. They found that an increase in the tip clearance would result in higher pressure fluctuation in the rotor region as well as different flow field and vortex dynamics near the tip region.

The experimental and numerical studies reviewed above have highlighted the complex dynamics of TLV and its associated cavitating structures. To understand this dynamics, numerical simulations can be a useful tool as it provides a complete access to the flow field, especially near the cavitating regions where it is difficult to get optically access in the experiments. However, the existing numerical studies used mostly RANS approaches which requires an ad-hoc modification to be able to predict the correct cavitation dynamics (Coutier-Delgosha et al., 2003). Furthermore, experimental studies by Wu et al. (2012) have shown that the flow in TLV is anisotropic and is controlled by several interacting shear layers. Capturing the dynamics of these shear layers and correct behavior of non-cavitating and cavitating TLV requires a scale-resolving approach, such as Large Eddy Simulation (LES). In this paper, numerical simulations of the axial water jet pump, AxWJ-2 (Michael et al., 2008), using an LES approach are presented. The simulations are performed on five different mesh resolutions and the predicted performance is compared with the experimental data available in Tan et al. (2015). Then the effect of mesh resolution on capturing TLV is discussed by comparing the numerical results with the experimental data in Li et al. (2016). Furthermore, the results from the cavitating simulation is presented and the effect of cavitation on the structure of TLV is discussed in detail.

NUMERICAL SET-UP

In this study, a modified version of the interPhaseChangeFoam solver from the OpenFOAM-2.2.x framework (Weller et al., 1998) is used to obtain the numerical results. This solver has been developed and validated by Huuva (2008), Bensow and Bark (2010), Lu et al. (2010), and Asnaghi et al. (2017). The governing equations are the incompressible Navier Stokes equations for two-phase (water-vapor) isothermal flows. Using a homogeneous mixture assumption and applying LES low pass filter (Arabnejad et al., 2019), the filtered equations for the mixture of water-vapor can be written as,

$$\frac{\partial}{\partial t}(\bar{\rho}) + \nabla \cdot (\bar{\rho}\tilde{\mathbf{u}}) = 0, \tag{1}$$

$$\frac{\partial}{\partial t}(\bar{\rho}\tilde{\mathbf{u}}) + \nabla \cdot (\bar{\rho}\tilde{\mathbf{u}} \otimes \tilde{\mathbf{u}}) + \nabla \cdot ([\bar{p}\mathbf{I} - \bar{\tau}]) + \nabla \cdot (\tau_{sgs}) = 0, \tag{2}$$

where $\bar{\rho}$, $\tilde{\mathbf{u}}$, and $\bar{p}$ are, respectively, the phasic filtered density, the Favre phasic filtered velocity vector, and the phasic filtered pressure, $\mathbf{I}$ is the identity tensor, $\bar{\tau}$ is viscous stress tensor and τ_{sgs} is the sub-grid scale tensor in the mixture momentum equations. Adopting the homogeneous mixture assumption and assuming that dynamic viscosity in each phase, μ^k, is constant, the mixture viscous stress tensor, $\bar{\tau}$, can be obtained from,

$$\bar{\tau} = (\sum_{k=1}^{2} \alpha^k \mu^k)\bar{S}, \tag{3}$$

where $\bar{S}$ is the mixture strain tensor. To account for the effect of the sub-grid scale turbulence, we adopted the wall-adapting local eddy-viscosity (WALE) model proposed by Nicoud and Ducros (1999). In this model, the sub-grid scale tensor, τ_{sgs}, is written as,

$$\tau_{sgs} - \frac{2}{3}k_{sgs}\mathbf{I} = -2\nu_{sgs}\bar{S}, \tag{4}$$

where k_{sgs} is the sub-grid kinetic energy and ν_{sgs} is the sub-grid scale turbulent viscosity which can be obtained from,

$$\nu_{sgs} = C_k \Delta \sqrt{k_{sgs}}. \tag{5}$$

In the above equation, Δ is the cell length scale, C_k, the model constant, is assumed to be 1.6, and k_{sgs}, the sub-grid kinetic energy, can be calculated from,

$$k_{sgs} = \left(\frac{C_w^2 \Delta}{C_k}\right)^2 \frac{(\tilde{S}^d \tilde{S}^d)^3}{\left(\left(\tilde{S}\tilde{S}\right)^{5/2} + \left(\tilde{S}^d \tilde{S}^d\right)^{5/4}\right)^2}, \tag{6}$$

where $\tilde{S}$ and $\tilde{S}^d$ are, respectively, the resolved-scale strain rate tensor and traceless symmetric part of the square of the velocity gradient tensor, and C_w, the model constant, is assumed to be 0.325.

For the cavitating simulation, the cavitation dynamics is captured by Transport Equation Modelling (TEM), where a transport equation for the liquid volume fraction, α^l, is solved. This equation reads,

$$\frac{\partial}{\partial t}(\alpha^l \bar{\rho}^l) + \nabla \cdot (\alpha^l \bar{\rho}^l \tilde{\mathbf{u}}) = \dot{m}, \tag{7}$$

where $\dot{m}$ is the mass transfer term which accounts for vaporization and condensation. Here, the Schnerr-Sauer model (Sauer and Schnerr, 2000) is used for this term. The mass transfer term is written as the summation of condensation, $\dot{m}_{\alpha_c^l}$, and vaporization, $\dot{m}_{\alpha_v^l}$, terms as,

$$\dot{m} = \alpha^l \left(\dot{m}_{\alpha_v^l} - \dot{m}_{\alpha_c^l}\right) + \dot{m}_{\alpha_c^l}, \tag{8}$$

where $\dot{m}_{\alpha_v^l}$ and $\dot{m}_{\alpha_c^l}$ are obtained from

$$\dot{m}_{\alpha_c^l} = C_c \alpha^l \frac{3\bar{\rho}^l \bar{\rho}^v}{\bar{\rho} R_B} \times \sqrt{\frac{2}{3\bar{\rho}^l}} \sqrt{\frac{1}{|\bar{p} - p_v|}} max\left(\bar{p} - p_v, 0\right), \tag{9}$$

$$\dot{m}_{\alpha_v^l} = C_v \left(1 + \alpha_{Nuc} - \alpha^l\right) \frac{3\bar{\rho}^l \bar{\rho}^v}{\bar{\rho} R_B} \times \sqrt{\frac{2}{3\bar{\rho}^l}} \sqrt{\frac{1}{|\bar{p} - p_v|}} min\left(\bar{p} - p_v, 0\right). \tag{10}$$

In equations 9 and 10, C_c and C_v are set to 1, p_v is the vapor pressure, α_{Nuc} is the initial volume fraction of nuclei, and R_B is the radius of the nuclei which is obtained from

$$R_B = \sqrt[3]{\frac{3}{4\pi n_0} \frac{(1 + \alpha_{Nuc} - \alpha^l)}{\alpha^l}}. \tag{11}$$

The initial volume fraction of nuclei is calculated from

$$\alpha_{Nuc} = \frac{\frac{\pi n_0 d_{Nuc}^3}{6}}{1 + \frac{\pi n_0 d_{Nuc}^3}{6}}, \tag{12}$$

where the average number of nuclei per cubic meter of liquid volume, n_0, and the initial nuclei diameter, d_{Nuc}, are assumed to be 10^{12} and 10^{-5} m, respectively.

Discretization scheme and solution algorithm

The convective terms in the momentum equations are discretized using a second order upwind scheme by Warming and Beam (1976). The diffusion terms in the momentum equations are discretized using linear scheme. The convective term in the liquid fraction is discretized using a first order upwind scheme. For time discretization, a second order implicit scheme is used. The discretized equations are solved using a pressure-based PIMPLE approach. More detail about the solution procedure can be found in Asnaghi et al. (2017) and Bensow and Bark (2010).

Computational domain

The AxWJ-2 axial water jet pump (Michael et al., 2008) is selected for the simulations in this paper. Figure 2 and Table 1 present, respectively, a schematic view of the pump and a summary of relevant data for this pump. As it can be seen in Table 1, the actual tip clearance where the measurements are done, is 0.9 mm while the nominal tip clearance is 0.7 mm. The reason for this difference is that there is a misalignment between the axis of the rotor and the centreline of the shroud in the experimental set-up according to Li et al. (2016). This misalignment means that the tip clearance of a blade varies as it rotates and that in each rotation, the tip clearance of each blade is equal to 0.9 mm only at one blade position. In order to obtain the converged statistics for this position, a larger number of rotor revolutions was used in the experiment. However, running this larger number of rotor revolutions is not possible in the numerical simulation due to high computational cost. Therefore, in order to lower the computational cost, the diameter of the shroud in the simulation is expanded by 0.4 mm so that the tip clearance is 0.9 mm for all blades during one revolution. It should be mentioned that the edges of the rotor blades in the experiment by Li et al. (2016) are rounded. Since the radius of the rounded edges were not reported, sharp edges are used in the

Table 1: Summary of relevant data for AxWJ-2 axial water jet pump.

D_1	305.2 mm
D_2	213.4 mm
D_{rotor}	303.8 mm
Number of rotor blades n_R	6
Number of stator blades n_S	8
Nominal tip clearance h	0.7 mm
Actual tip clearance h	0.9 mm
Angular speed of the rotor Ω	900 RPM

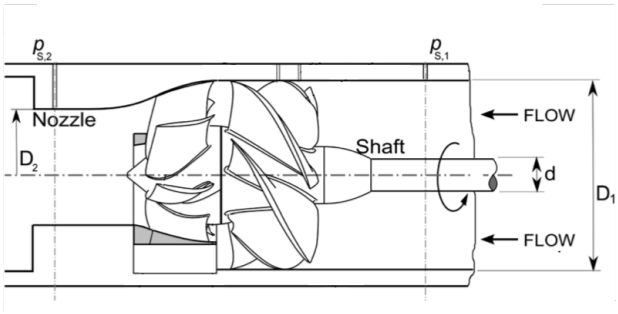

Figure 2: Sketch of the AxWJ-2 axial water jet pump (Tan et al., 2015).

Table 2: Description of the grids in rotor region.

Grids	Size	n_1	n_2	n_3	n_4	n_5	n_r	n_c	y^+
CM	1.9M	10	10	8	14	39	56	58	180
MM	5.0M	15	15	12	21	53	75	84	135
FM	12.5M	20	20	16	28	68	104	116	90
FMRefAll	46.6M	40	40	32	56	136	152	232	45
FMRefOne	19.7M	40	40	32	56	136	152	232	45

simulation. These differences between the experimental and numerical geometries should be considered while comparing the numerical results with the experiment.

Figure 3(a) shows the computational domain used in this study. The computational domain is extended $10D_1$ upstream and downstream of the pump to reduce the interaction between the flow in the pump and the inlet and outlet boundary conditions. The domain is divided into three regions, inlet_pipe, rotor, and stator_outlet_pipe. Cyclic Arbitrary Mesh Interfaces (AMI) are used for the boundaries between these regions. For the inlet_pipe, a fully structured grid is used and the mesh is refined near the casing and the shaft to capture the boundary layers near these surfaces. The tangential resolution is, however, not fine enough for a wall-resolved LES, therefore wall functions based on Spalding's law (Spalding, 1961) are used for these surfaces. The mesh in the rotor and stator is divided into two regions with different types of mesh. The regions near the rotor blades, the hub, and the shroud are discretized with a structured hexahedral mesh, and the region in the middle of the passage is discretized with an unstructured mesh. The mesh topology in the rotor region is shown in Figure 3(b). In order to study the effect of mesh resolution, three base-line grids for the rotor region, CM, MM, and FM (described in table 2), are created. These grids have, respectively, 1.9, 5.0. and 12.5 million cells. These grids are created using Pointwise V18.2 grid generation software. To further increase the mesh resolution in the tip leakage region, the resolution of this region in the FM mesh is refined locally using the refineHexMesh utility in OpenFOAM. The refinement is performed around one blade (FMRefOne in table 2) and all of the blades (FMRefAll in Table 2). The refinement zone covers the tip of blade from $r/R = 0.8$ to $r/R = 1.0$ and in case of refinement around one blade, it is extended angularly 50 degrees in the suction side and 30 degrees in the pressure side direction of the selected blade (see Figure 3(b)). Table 2 presents the grid specifications for each grid. In this table, the locations of n_{1-5} are defined in Figure 3(b), n_r and n_c are the number of the grids on the blade in radial and chord-wise directions and y^+ is non-dimensional wall distance of the first cell on the blade based on the tip velocity of the blade and the diameter of the rotor. It should be mentioned that wall functions based on Spalding's law (Spalding, 1961) are applied for all wall surfaces in the simulations except for the rotor shroud in the FMRefOne and FMRefAll simulations where the resolution is high enough to capture the boundary layer.

In order to check whether the mesh resolutions described in Table 2 are adequate for LES, the ratio

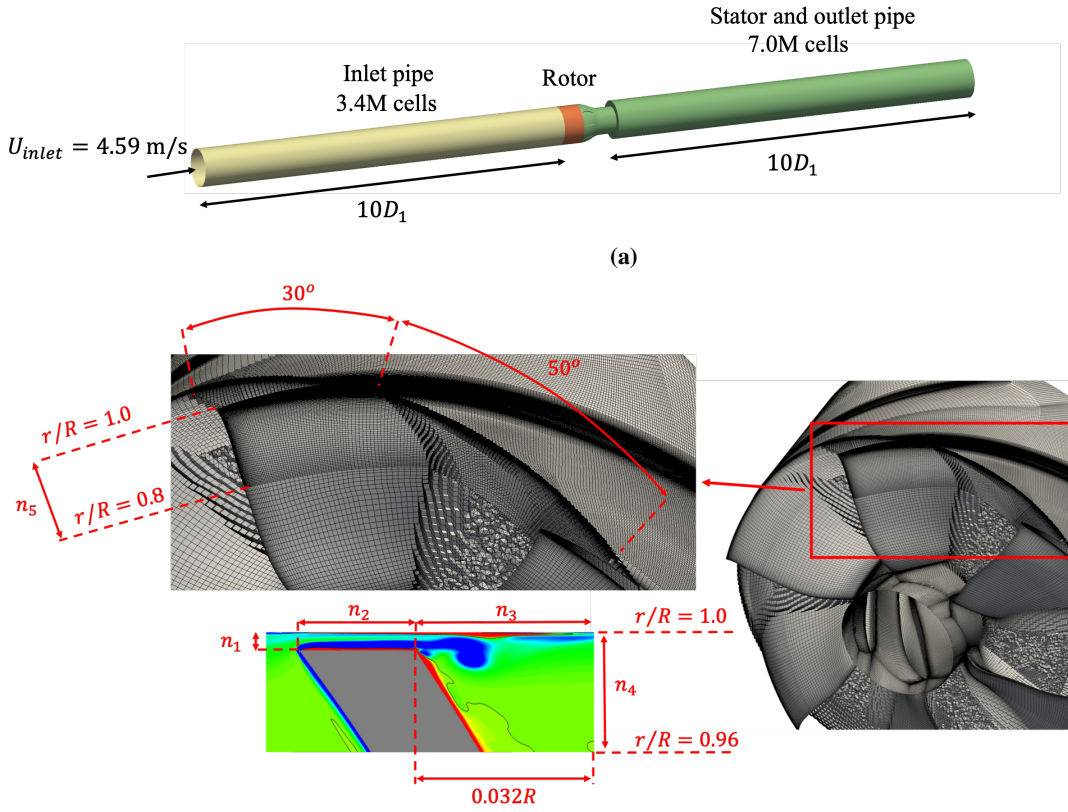

Figure 3: (a) Computational domain and (b) Mesh topology in the rotor region.

between the modeled sub-grid scale kinetic energy and total kinetic energy is estimated based on the method proposed by Pope (2000). This ratio is defined as,

$$M = \frac{k_{sgs}}{k_{sgs} + k_{res.}}, \tag{13}$$

where k_{sgs} is the modeled sub-grid scale kinetic energy obtained from equation 6 and $k_{res.}$ is the resolved kinetic energy which is obtained from,

$$k_{res.} = \frac{1}{2}\sum_{i=1}^{3} u_{rms,i}^2, \tag{14}$$

where $u_{rms,i}$ is the root mean square of velocity fluctuations in the direction i. Figure 4 shows the distribution of the ratio M on several meridional planes where the TLV occurs in for simulations using coarsest and the finest mesh in Table 2 (CM and FMRefOne). It can be seen that this ratio is lower than 10 percent in these simulations, indicating more than 90 percent of the kinetic energy is resolved, therefore the mesh resolutions described in Table 2 are adequate for LES.

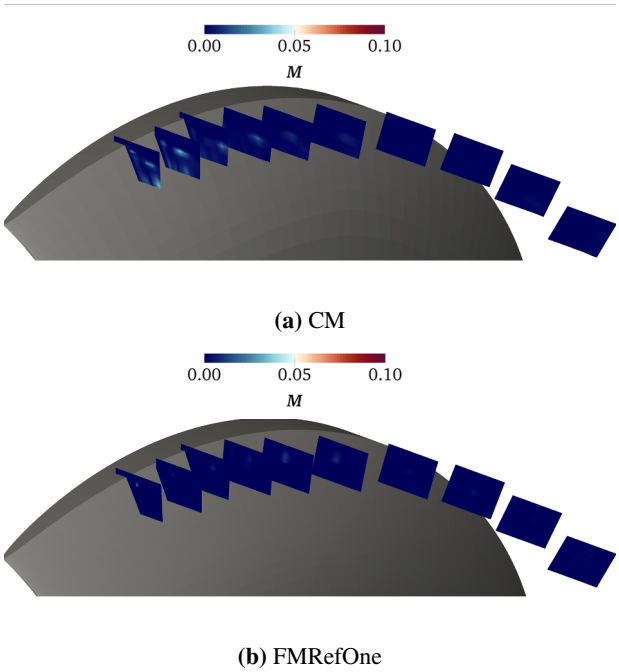

Figure 4: The ratio between the modeled sub-grid scale kinetic energy and total kinetic energy in the simulations using CM and FMRefOne mesh resolutions.

RESULTS

The results section is divided into two parts. The first part is devoted to investigating the effect of mesh refinement on performance prediction and capturing of non-cavitating TLV and in the second part, the structure of non-cavitating and cavitating TLVs are compared and the effect of cavitation on the structure of TLV is discussed.

Effect of mesh refinement

Table 3 presents the performance of the pump predicted by numerical simulations with different mesh resolutions. Similar to Tan et al. (2015), the performance of the pump is shown as the head rise coefficient, ψ. This coefficient is defined as,

$$\psi = \frac{p_{s,2} - p_{s,1} + \frac{\rho}{2}\left[\left(\frac{Q}{A_2}\right)^2 - \left(\frac{Q}{A_1}\right)^2\right]}{\rho n^2 D_1^2}, \qquad (15)$$

where Q is the volumetric flow rate in m^3/s and n is the shaft rotation speed in revolutions per seconds, and $p_{s,1}$, $p_{s,2}$, A_1, and A_2 are, respectively, the static pressures near the casing wall and the flow cross-section areas at location 1 and location 2, shown in Figure 2. In this paper, we studied the pump at the flow coefficient, $\varphi = Q/nD_1^3 = 0.75$ where the experimentally measured head rise coefficient, $\psi_{Exp.}$, is equal to 2.46 according to Tan et al. (2015). Comparison between $\psi_{Exp.}$ and the numerical head rise coefficients in Table 3, $\psi_{Num.}$, indicates that despite the modification made in the computational domain (explained in Numerical set-up section), the predicted performance is in a good agreement with the experimental data. It can also be seen in Table 3 that by refining the mesh resolution in the entire rotor (CM, MM, and FM simulations), the predicted performance changes less than 5 percent. This change for the cases where the refinement is only applied to the tip region is even less significant as the difference between the predicted performance in FM, FMRefAll, and FMRefOne simulations is less than 1 percent. However, as it will be shown later, by applying the mesh refinement around the tip, the TLV can be captured with more detail. The small difference between the predicted performance by FM, FMRefAll, and FMRefOne, simulation indicates that these captured details do not affect the performance of the pump.

Table 3: Performance of the pump predicted by numerical simulations

Simulations	Mesh Size	$\psi_{num.}$	% error
CM	1.9M	2.359	4.1
MM	5.0M	2.339	4.9
FM	12.5M	2.462	0.1
FMRefAll	46.6M	2.440	0.8
FMRefOne	19.7M	2.458	0.1
Exp.	-	2.46	-

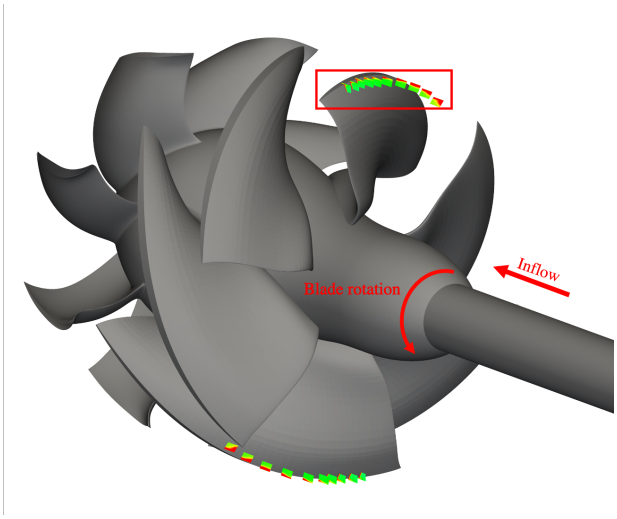

Figure 5: Locations of meridional planes used for the comparison between numerical results and experimental data in Figure 6.

In order to study the effect of mesh resolution on capturing the TLV, the time averaged tangential vorticity and velocity fields on several meridional planes obtained by different mesh resolutions are compared with the experimental data by Li et al. (2016) in Figure 6. Figure 5 shows the location of these planes with respect to the rotor blade. In the experimental images, three regions with high vorticity generation, denoted by A, B, and C in Figure 6(a), can be seen. According to Wu et al. (2012), the high vorticity value in regions A, B, and C are, respectively, due to the shear layer between the reverse flow exiting the tip gap and the flow inside the passage, the boundary layer separation in the tip leakage flow near the rotor casing, and the core of TLV. It can be seen in the experimental images that as the TLV travels in the passage, the tangential vorticity in the TLV decays and this decay coincides with the increase in the tangential velocity. In the coarse mesh results (Figure 6(b)), the high

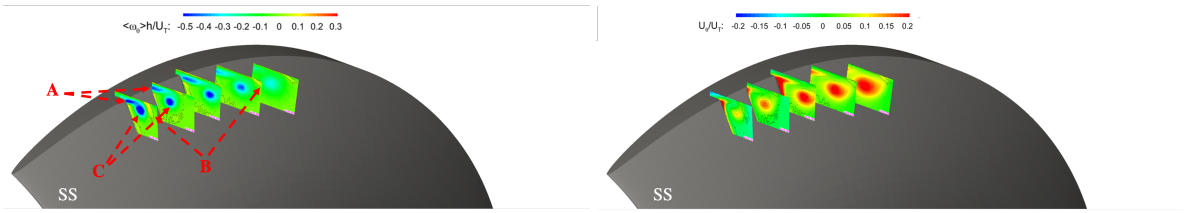

(a) SPIV by Li et al. (2016)

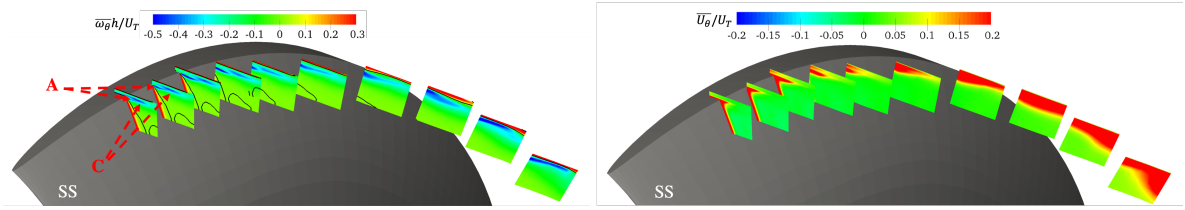

(b) CM

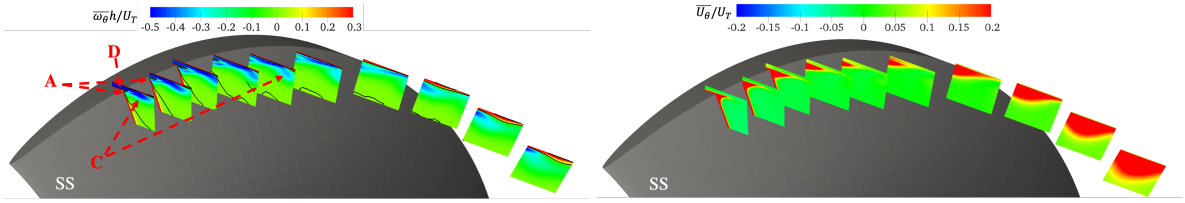

(c) MM

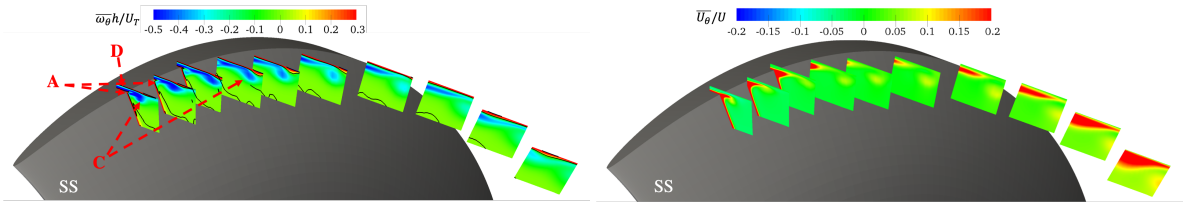

(d) FM

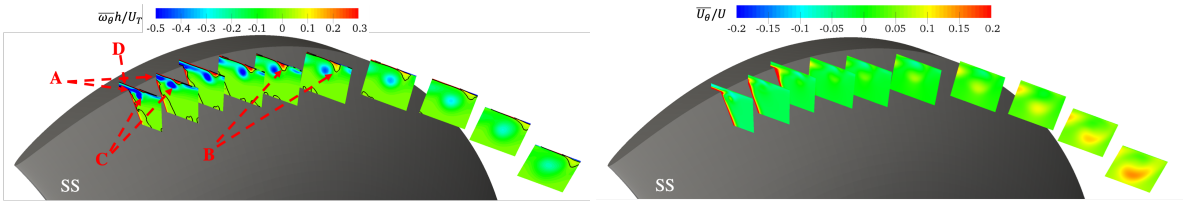

(e) FMRefOne

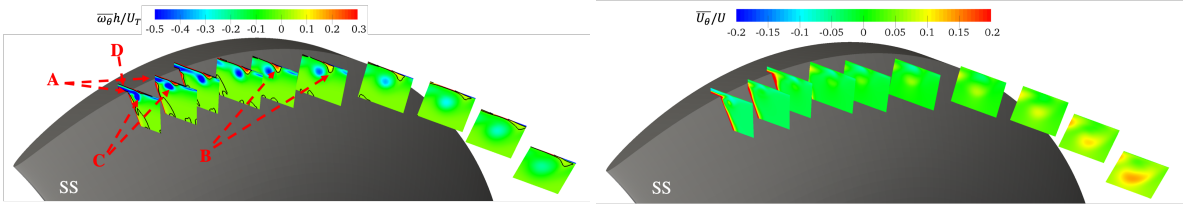

(f) FMRefAll

Figure 6: Comparison between the time averaged tangential vorticity field and time averaged tangential velocity on different meridional planes in the experimental SPIV and numerical simulations obtained with different mesh resolutions.

vorticity due the shear layer (region A) and the trace of the TLV core (region C) can be seen. However, the TLV has the form of a vortex sheet instead of a cylindrical vortex. It is also evident in the coarse mesh results that the boundary layer near the shroud remains attached as the mesh is too coarse to capture the boundary layer separation. In the medium mesh results (Figure 6(c)), the shear layer in region A and the TLV core in region C can be seen but these regions are not separated as compared to the experimental images. Similar to the coarse mesh results, no sign of boundary layer separation can be detected, but the boundary layer is thicker in the planes closer to the trailing edge. The distribution of the tangential velocity in the coarse mesh and medium mesh simulations shows that the tangential velocity increases along the trajectory of the TLV but this increase does not occur in the plane where the tangential vorticity of the TLV decays. Similar vortex dynamics can be seen in the results from the fine mesh (Figure 6(d)) with the difference that the thickening of the boundary layer near the casing occurs in the planes closer to the leading edge. In contrast to the results from CM and MM simulations, the increase in the tangential velocity can be seen in the planes where the tangential vorticity in the TLV decays. In the results from the fine meshes with refinement at the tip (Figures 6(e) and 6(f)), the captured TLVs have the main feature of the TLV in the experiment. In the simulations, the main core of the TLV is attached to the shear layer in the closest plane to the leading edge, which means that the core of TLV is fed by the structures in the shear layer. As the TLV travels in the passage, it becomes disconnected from the shear layer. The same behavior can be seen in the experimental images. Furthermore, the vortex in the simulations has the same cylindrical shape as the experiment and the high value of vorticity in the core of the TLV decays as the vortex travels in the passage. In these simulations, the boundary layer separation can be captured and similar to the experiments, at the planes which the decay in the tangential vorticity occurs, an increase in tangential velocity can be seen. The comparison between the results from the fine mesh with refined tip around one blade and all blades (Figures 6(e) and 6(f)) shows that almost identical TLV dynamics can be captured by two mesh resolution which indicates that there is an insignificant interaction between the TLVs formed on the neighboring blades.

The numerical results in Figure 6 show the existence of a region with high value of vorticity, denoted by D, in the tip gap, while this region cannot be seen in the experiment. To identify the reason for this difference, the streamlines and the vorticity distribution on the third plane from the leading edge in Figure 6(e) are shown in Figure 7. The streamlines show that as the leakage flow enters the tip gap, it separates from the sharp edge at the pressure side. Inside this separated flow, there is a shear layer which generates the high value of vorticity in region D. As mentioned in the Numerical step-up section, the edges of the rotor blade at tip were rounded in the experiment, therefore a weaker separation at the edge of the pressure side is expected. This weaker separation can explain the lower value of vorticity in the tip gap in the experimental results compared to the simulation.

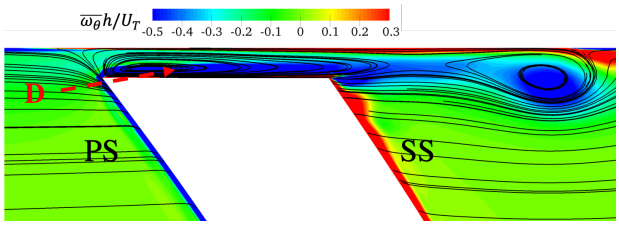

Figure 7: Flow separation at the edge of pressure side of the rotor blade. The contours show the non-dimensional time averaged tangential velocity.

Effect of cavitation

In order to study the effect of cavitation on the structure of TLV, a cavitating simulation is performed using the fine mesh with one refined blade (FMRefOne in Table 2). In this simulation, the flow rate coefficient is the same as in the non-cavitating simulation and the cavitation number, $\sigma = (p_{1,s} - p_v)/0.5\rho U_T^2$, is set to 1.62. Table 4 compares the predicted performance in the non-cavitating and cavitating simulations. This comparison shows that cavitation has insignificant effect on the performance at the condition studied here. This is expected according to the experimental study by Tan et al. (2015), as this flow condition is not close to cavitation break-down.

Table 4: Comparison between the predicted performance in the non-cavitating and cavitating simulations.

Simulations	mesh size	σ	$\psi_{num.}$
FMRefOne	19.7M	∞	2.458
FMRefOneCav	19.7M	1.62	2.443

Figure 8 compares the cavitation regions in the high speed visualization by Tan et al. (2015) and current numerical simulation. The comparison shows that the current simulation set-up can capture the main feature of cavitating regions. In both simulation and experiment, there exists three main cavitating structures, (1) the sheet cavitation formed on the suction side of the blade, (2) the large-scale cavitating TLV, (3) the small-scale cavitating structures formed downstream of the cavitating TLV. Figure 8 shows that the cavitating TLV consists of a cavity

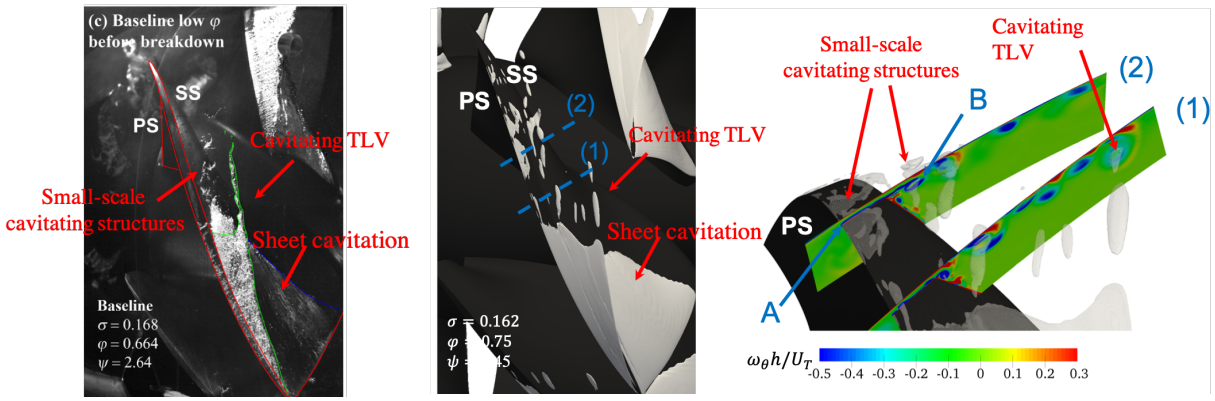

(a) HSV by Tan et al. (2015)

(b) FMRefOneCav

Figure 8: Comparison between cavitating regions in the numerical simulation and high speed visualization by Tan et al. (2015)

attached to the blade followed by a cavitating vortex at its tail. It can also be seen that the attached cavity starts from the edge of the pressure side, where according to the non-cavitating simulation results, a separation zone exists. The small cavitating structures formed downstream of the main cavitating TLV are shown in the close-up view of Figure 8(b). The distribution of the tangential vorticity on two planes is also depicted in this figure. From this distribution and the position of small-scale cavitating structures, it is evident that these structures are formed in two regions with a high value of tangential vorticity. The first region is the separation zone at the edge of blade on the pressure side (A in the close-up view) and the second one is the shear layer attached to the suction side of the blade (B in the close-up view). Figure 8(b) also shows that the cavitating vortices are detached from both regions and transported into the passage.

Figure 9(a) shows the time-averaged tangential vorticity on several meridional planes in the cavitating simulation. The positions of these meridional planes with respect to the cavitating structures and the distribution of liquid volume fraction on these planes are shown in Figure 9(c). Comparison between this vorticity distribution and the one in the non-cavitating simulation presented in Figure 6(e), indicates that cavitation has a significant effect on the structure of the TLV. In the first six planes of

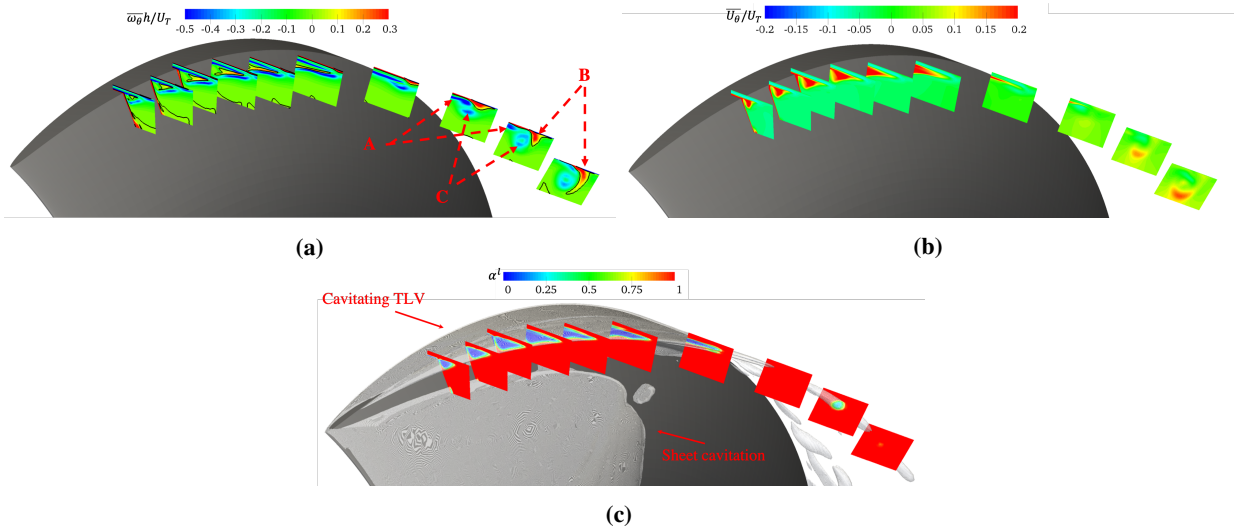

(a)

(b)

(c)

Figure 9: The structure of cavitating TLV, a) distribution of time averaged tangential vorticity, b) the time averaged tangential velocity on different meridional planes, and c) iso-surface of vapor fraction and the distribution of vapor fraction on different meridional planes.

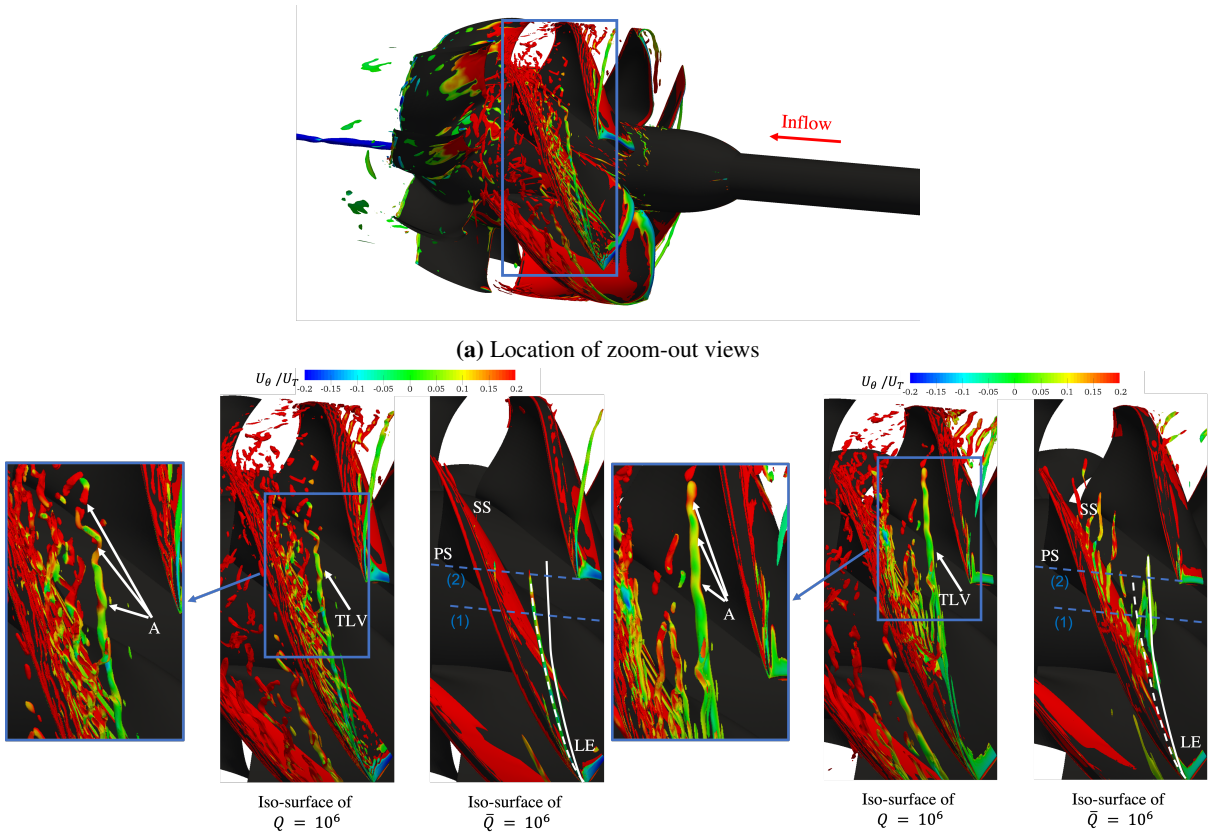

(a) Location of zoom-out views

(b) FMRefOne

(c) FMRefOneCav

Figure 10: Vortical structures identified by iso-surface of instantaneous Q criteria and the time averaged Q criteria, a) location of zoom-out views, b) non-cavitating simulation, c) cavitating simulation (White dashed line: trajectory of non-cavitating TLV, white solid line: trajectory of cavitating TLV)

Figure 9(a) where vapor phase exists according to Figure 9(c), the high negative value of tangential vorticity can be seen on the interface of the cavitating TLV instead of the three regions in the non-cavitating simulation shown in Figure 6(e). It can also be seen that the boundary layer on the shroud in these planes remains attached in the cavitating simulation. However, in the last four planes where a cavitating vortex is detached from the main cavitating TLV, the distribution of time averaged tangential vorticity becomes similar to the non-cavitating one. In these planes, the same three high vorticity regions can be seen and the tangential vorticity decays as the cavitating vortex travels downstream. Figure 9(b) presents the time averaged tangential velocity on the same meridional planes as Figure 9(a). In the first six planes, the cavitating TLV has a tangential velocity very close to the blade tangential velocity at the tip. This is different from the non-cavitating TLV where in the first six planes, the main core of TLV has almost no tangential velocity. It can also be seen in Figure 9(b) that the tangential velocity in the detached cavitating vortex (the last four planes in Figure 9(b)) is small right after the detachment point but increases to a higher value in the downstream end of the vortex. Similar to the non-cavitating TLV shown in Figure 6(e), this increase in the tangential velocity coincides with the decay in the tangential vorticity.

As shown in both non-cavitating and cavitating simulations, the increase in time-averaged tangential velocity around the TLV and decay in its tangential vorticity occur at the same position in the passage. Wu et al. (2012) suggested that both phenomena are due to the bursting of TLV. To confirm this, vortical structures around the tip of the blade in the non-cavitating and cavitating conditions are shown in Figure 10. The vortical structures in this figure are identified by iso-surfaces of instantaneous and time averaged Q-criteria and these iso-surfaces are coloured by tangential velocity. The iso-surface of Q shows that the bursting of the vortex can be seen in both non-cavitating and cavitating conditions (close-up views in Figure 10). It is noted that ahead of the vortex bursting, the trajectory of the TLV is almost a straight line and the tangential velocity is small around

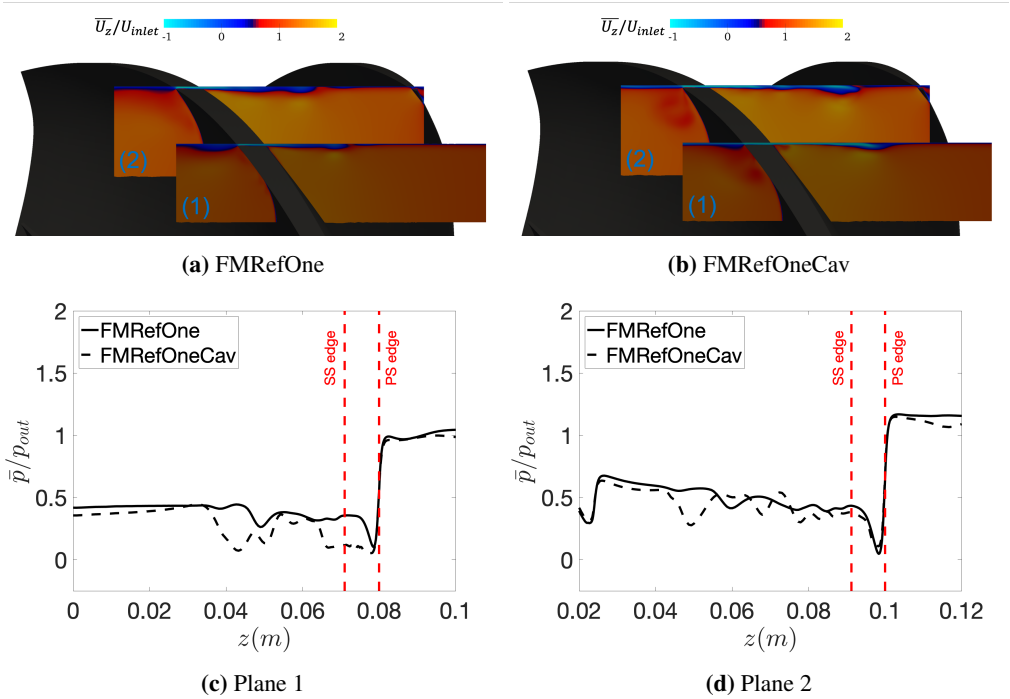

(a) FMRefOne

(b) FMRefOneCav

(c) Plane 1

(d) Plane 2

Figure 11: The leakage flow on two meridional for a) non-cavitating and b) cavitating conditions and c,d) the pressure along the intersction of the planes with the shroud (The location of the planes with respect to the main TLV is shown in Figure 10).

the vortex. When there is a kink in the trajectory of TLV due to vortex bursting (A-regions in the close-up views of Figure 10), the tangential velocity around the vortex increases. Furthermore, the vortex is unsteady after the vortex bursting and due to the kinks, it develops components different than tangential direction. This unsteadiness and the redirection of vorticity contributes to the decay in the time averaged tangential vorticity in Figures 9(a). It can also be seen in the figure that small structures are detached from the edge of the blade on the suction side after the detachment of the main TLV from the leading edge. These small structures are formed in the shear layer between the leakage flow and the flow in the passage (region A in Figures 6(e) and 9(a)). Similar to the TLV after the vortex bursting, the small structures have tangential velocity close to the blade velocity. The iso-surface of the time-averaged Q-criteria shows that the time-averaged trajectory of the TLV in non-cavitating (white dashed lines in Figure 10(b)) and cavitating (white solid lines in Figure 10(b)) conditions is different. In order to identify the reason for this difference, Figures 11(a) and 11(b) show the time average axial velocity near the tip region on two meridional planes for the cavitating and non-cavitating conditions. In both conditions, a region with negative values of axial velocity can be seen. This region, which originates from the tip gap, is due to the presence of the leakage flow from the pressure side of the blade to its suction side. Comparison between the tip leakage flow in the non-cavitating and cavitating condition shows that this region with negative axial velocity in the cavitating condition is larger which indicates that the tip leakage flow is stronger in the cavitating condition. This stronger tip leakage flow is responsible for the change in the trajectory of TLV as it can penetrate deeper into the passage. Figures 11(c) and 11(d) shows the time-averaged pressure on the casing for the two planes in Figures 11(a) and 11(b). It can be seen that in cavitating conditions the pressure difference between the suction side and pressure side of the blade is higher. As this pressure difference is the driving force for the leakage flow, it is expected that the tip leakage flow is stronger in cavitating condition.

CONCLUSION

In this paper, Large Eddy Simulation (LES) of the AxWJ-2 pump from Johns Hopkins University is presented. A series of non-cavitating simulations are performed using different mesh resolutions and the results are compared with the experimental data. Furthermore, a cavitating simulation is performed and the effect of cavitation on the structure of Tip Leakage Vortex (TLV) is investigated. The conclusions may be summarized as

follows:

- The comparison between the structure of non-cavitating TLV in the simulations using different mesh resolutions reveals that a mesh refinement region with at least 40 cells in tip gap is needed to capture the correct structure of non-cavitating TLV in the experiment.
- For non-cavitating TLVs, it is also shown that the refinement region can be applied on only one blade as there is a weak interaction between the tip leakage flow of the neighboring blades.
- The cavitating simulation using the grid with the same mesh refinement also shows that the simulation is capable of reproducing both small-scale and large-scale cavitating structures in the experiment.
- By comparing the structure of non-cavitating and cavitating TLVs, it is shown that cavitation has a significant effect on the structure of TLV. While the high value of vorticity in non-cavitating TLV occurs in three regions, the shear layer attached to the blade, the separated boundary layer separation on the casing, and the core of the TLV, the cavitation interface in the cavitating TLV is mostly associated with the high value of tangential vorticity. It is also shown that the presence of cavitation leads to a higher pressure difference between the pressure side and the suction side of the blade. As a result of this higher pressure difference, the tip leakage flow in the cavitating condition is stronger, therefore it can penetrate deeper in the passage. This in turn changes the trajectory of the main TLV.
- Both non-cavitating and cavitating simulations show that, similar to the SPIV data by Li et al. (2016), a decay in the tangential vorticity and an increase in the tangential velocity can be seen along the trajectory of the TLVs. Analysis of the numerical results reveals that these two phenomena occurs due to the bursting of the vortex where the TLV becomes unsteady and its trajectory deviates from a straight line.

In the flow conditions studied in this paper, the TLVs and their resultant cavitating structures are not large enough to cause cavitation breakdown. The experimental study by Tan et al. (2015), however, shows that at certain flow conditions, the cavitating TLV leads to the formation of Perpendicular Cavitating Vortices (PCV) which are responsible for the onset of cavitation breakdown. As a future work, the flow conditions corresponding to cavitation breakdown will be simulated using the numerical step-up presented in this paper and the mechanism for the generation of PCVs will be explained.

ACKNOWLEDGEMENTS

Financial support for this work has been provided by Kongsberg Maritime through the University Technology Centre in Computational Hydrodynamics hosted at the Division of Marine Technology, Department of Mechanics and Maritime Sciences at Chalmers. The simulations were performed on resources at Chalmers Centre for Computational Science and Engineering (C3SE) as well as National Supercomputer Center at Linköping University (NSC) provided by the Swedish National Infrastructure for Computing (SNIC).

REFERENCES

M.H. Arabnejad, A. Amini, R.E. Bensow, and M. Farhat. Numerical and experimental investigation of shedding mechanisms from leading-edge cavitation. International Journal of Multiphase Flow, 119: 123–143, 2019.

A. Asnaghi, A. Feymark, and R.E. Bensow. Improvement of cavitation mass transfer modeling based on local flow properties. International Journal of Multiphase Flow, 93:142–157, 2017.

F. Avellan. Introduction to cavitation in hydraulic machinery. In The 6th International Conference on Hydraulic Machinery and Hydrodynamics, Timisoara, Romania, pages 21–22, 2004.

R.E. Bensow and G. Bark. Implicit LES predictions of the cavitating flow on a propeller. Journal of Fluids Engineering, 132(4):041302, 2010.

O. Coutier-Delgosha, R. Fortes-Patella, and J. Reboud. Evaluation of the turbulence model influence on the numerical simulations of unsteady cavitation. Journal of Fluids Engineering, 125(1):38–45, 2003.

J. Feng, X. Luo, P. Guo, and G. Wu. Influence of tip clearance on pressure fluctuations in an axial flow pump. Journal of Mechanical Science and Technology, 30(4):1603–1610, 2016.

T. Huuva. Large eddy simulation of cavitating and non-cavitating flow. PhD thesis, Chalmers University of Technology, 2008.

R. Laborde, P. Chantrel, and M. Mory. Tip clearance and tip vortex cavitation in an axial flow pump. Journal of Fluids Engineering, 119(3):680–685, 1997.

Y. Li, D. Tan, H. Chen, and J. Katz. Stereoscopic piv measurement of the flow in the tip region of an

axial waterjet pump. In 16th International Symposium on Transport Phenomena and Dynamics of Rotating Machinery, 2016.

N. Lu, R. E. Bensow, and G. Bark. LES of unsteady cavitation on the delft twisted foil. Journal of Hydrodynamics, Ser. B, 22(5):784–791, 2010.

T. Michael, S. Schroeder, and A. Becnel. Design of the ONR AxWJ-2 axial flow water jet pump. Technical report, Hydromechanics Department Report No. NSWCCD-50TR-2008/066., 2008.

R.L. Miorini, H. Wu, and J. Katz. The internal structure of the tip leakage vortex within the rotor of an axial waterjet pump. Journal of Turbomachinery, 134(3): 031018, 2012.

F. Nicoud and F. Ducros. Subgrid-scale stress modelling based on the square of the velocity gradient tensor. Flow, turbulence and Combustion, 62(3):183–200, 1999.

S.B. Pope. Turbulent Flows. Cambridge University Press, 2000. doi: 10.1017/CBO9780511840531.

J. Sauer and G. H. Schnerr. Unsteady cavitating flow-a new cavitation model based on a modified front capturing method and bubble dynamics. In Proceedings of 2000 ASME fluid engineering summer conference, volume 251, pages 1073–1079, 2000.

D. Spalding. A single formula for the law of the wall. Journal of Applied Mechanics, 28(3):455–458, 1961.

D. Tan, R. Miorini, J. Keller, and J. Katz. Flow visualization using cavitation within blade passage of an axial waterjet pump rotor. In ASME 2012 Fluids Engineering Division Summer Meeting collocated with the ASME 2012 Heat Transfer Summer Conference and the ASME 2012 10th International Conference on Nanochannels, Microchannels, and Minichannels, pages 395–404. American Society of Mechanical Engineers, 2012.

D. Tan, Y. Li, I. Wilkes, E. Vagnoni, R. Miorini, and J. Katz. Experimental investigation of the role of large scale cavitating vortical structures in performance breakdown of an axial waterjet pump. Journal of Fluids Engineering, 137(11):111301, 2015.

R.F. Warming and R. M. Beam. Upwind second-order difference schemes and applications in aerodynamic flows. AIAA Journal, 14(9):1241–1249, 1976.

H. Weller, G. Tabor, H. Jasak, and C. Fureby. A tensorial approach to computational continuum mechanics using object-oriented techniques. Computers in Physics, 12 (6):620–631, 1998.

H. Wu, D. Tan, R. Miorini, and J. Katz. Three-dimensional flow structures and associated turbulence in the tip region of a waterjet pump rotor blade. Experiments in Fluids, 51(6):1721–1737, 2011.

H. Wu, R. L. Miorini, D. Tan, and J. Katz. Turbulence within the tip-leakage vortex of an axial waterjet pump. AIAA Journal, 50(11):2574–2587, 2012.

D. Zhang, L. Shi, W. Shi, R. Zhao, H. Wang, and B. van Esch. Numerical analysis of unsteady tip leakage vortex cavitation cloud and unstable suction-side-perpendicular cavitating vortices in an axial flow pump. International Journal of Multiphase Flow, 77:244–259, 2015a.

D. Zhang, W. Shi, D. Pan, and M. Dubuisson. Numerical and experimental investigation of tip leakage vortex cavitation patterns and mechanisms in an axial flow pump. Journal of Fluids Engineering, 137(12):121103, 2015b.

D. Zhang, W. Shi, B. van Esch, L. Shi, and M. Dubuisson. Numerical and experimental investigation of tip leakage vortex trajectory and dynamics in an axial flow pump. Computers & Fluids, 112:61–71, 2015c.